INTERNATIONAL JOURNAL FOR NUMERICAL METHODS IN FLUIDS
Int. J. Numer. Meth. Fluids 2010; **63**:638–650
Published online 10 July 2009 in Wiley InterScience (www.interscience.wiley.com). DOI: 10.1002/fld.2101

A boundary condition for arbitrary shaped inlets in lattice–Boltzmann simulations

K. Mattila[1,*,†], J. Hyväluoma[1], A. A. Folarin[2] and T. Rossi[3]

[1]*Department of Physics, University of Jyväskylä, P.O. Box 35, FI-40014 Jyväskylä, Finland*
[2]*Department of Oncology, University College London (Hampstead Campus), London, U.K.*
[3]*Department of Mathematical Information Technology, University of Jyväskylä, P.O. Box 35, FI-40014 Jyväskylä, Finland*

SUMMARY

We introduce a mass-flux-based inlet boundary condition for the lattice-Boltzmann method. The proposed boundary condition requires minimal amount of boundary data, it produces a steady-state velocity field which is accurate close to the inlet even for arbitrary inlet geometries, and yet it is simple to implement. We demonstrate its capability for both simple and complex inlet geometries by numerical experiments. For simple inlet geometries, we show that the boundary condition provides very accurate inlet velocities when $Re \lesssim 1$. Even with moderate Reynolds number, the inlet velocities are accurate for practical purposes. Furthermore, the potential of our boundary condition to produce inlet velocities which convincingly adapt to complex inlet geometries is highlighted with two specific examples. Copyright © 2009 John Wiley & Sons, Ltd.

Received 24 April 2008; Revised 26 March 2009; Accepted 4 May 2009

KEY WORDS: lattice–Boltzmann method; flow simulation; inlet boundary condition; vascular system

1. INTRODUCTION

It is argued that the lattice-Boltzmann method (LBM) is amenable for simulations in complex geometries [1, 2]. Typically such geometries are encountered in simulations of flow in porous media or suspension flows [3, 4]. Many pipe and vessel systems also comprise complex geometries for fluid flow simulations [5–10]. Our work to develop a new inlet boundary condition is motivated by flow simulations in vascular systems. Such systems can be highly complicated—in particular tumour vascular systems. Blood flow velocity in normal tissues is well known to be correlated with the vessel caliber [11, 12]; this correlation is lost in tumour vessels due to a substantial reduction of

*Correspondence to: K. Mattila, Department of Physics, University of Jyväskylä, P.O. Box 35, FI-40014 Jyväskylä, Finland.
†E-mail: kemattil@jyu.fi

Contract/grant sponsor: Academy of Finland; contract/grant number: 7117283

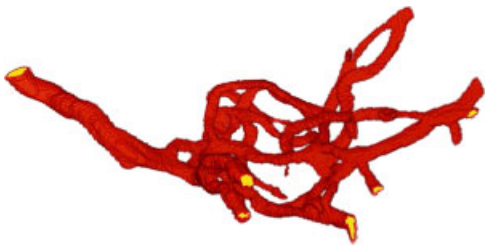

Figure 1. Segment of a tumour vascular system obtained with computed microtomography: scanning resolution is 3.6 μm.

structural organization caused by the abnormal vascular development in the tumour. Our ultimate aim is to investigate the flow characteristics of a range of tumour microvascular systems by simulating flows within high-resolution microcomputed tomography data sets of vascular corrosion casts. The dimensionless numbers in the simulations are matched with those determined by the literature values for blood flow at a similar scale. The literature provides following values: kinematic viscosity $5.48 \times 10^{-6}\,\mathrm{m}^2/\mathrm{s}$ [13], inlet blood flow velocity $1.0 \times 10^{-3}\,\mathrm{m/s}$ [14], and the characteristic length scales (mean vessel diameter) 20–40 μm. Together these situate the dimensionless Reynolds number for this flow regime between 3.65×10^{-3} and 7.3×10^{-3}.

The tumour vascular systems of our interest have single inlet vessel branching into smaller ones and thus have multiple outlet vessels. Figure 1 shows an example of such a system obtained with computed microtomography. At the inlets and outlets cross sections of the vessels can have arbitrary shapes, and the orientation of the vessels is nonuniform. This type of configuration is challenging, especially for inlet and outlet boundary conditions. First of all, the boundary data available, *a priori*, are typically very limited. For example, pressure boundary condition would require the definition of pressure difference between the single inlet and each of the outlets [15, 16]. In most cases, the pressure difference data for each outlet are difficult, if not impossible, to define or the pressure field can even be one of the desired results from the simulation.

Alternatively, one could apply velocity boundary conditions at the boundaries of the computational domain [4, 15–18]. Since the inlet vessel can have an arbitrary shape, setting an analytical velocity profile is not feasible: at best some approximation scheme could be devised. Often a uniform velocity profile is set for such inlets. A sophisticated approximation scheme for a velocity profile at the inlet is devised in Reference [19] by Freitas and Schröder. They assign a parabolic inflow profile based on the normal wall distances of the tracheal cross section. Furthermore, the shape of the inflow profile is oriented normal to the cross section. For the outlets, the velocity data are typically considered not available. So-called free-flow outlet boundary conditions are appealing, since they require no data for the boundaries [15, 20, 21]. However, the free-flow boundary conditions currently available are not completely understood and may produce velocity fields at the outlets which are unphysical—in particular if the outgoing vessels do not align with the faces of the computational domain. In spite of the known limitations, we choose to apply a free-flow boundary condition for the outlet in our numerical experiments.

Here our focus is on the inlet boundary condition. In essence, we introduce a scheme where a given average velocity is enforced at the inlet. The approach taken here leads to an expression for the inlet density (pressure) after which, and with some fundamental assumptions, local inlet velocities are readily available in LBM. Thus, the proposed inlet scheme can be categorized as a

DOI: 10.1002/fld

Dirichlet-type boundary condition. The novelty of this scheme is that the inlet density and local inlet velocities are free to evolve in time—only the average velocity is fixed. This relates our scheme to free-flow and open boundary conditions common in computational fluid dynamics. Finally, the time evolution will converge to a steady-state where the computed inlet velocity profile very accurately conforms to the inlet geometry and thereby, e.g. to analytical solutions if available. Two practical aspects motivate the use of our inlet scheme: there is no need to prescribe an inlet velocity profile (i.e. local velocities at the inlet) nor pressure differences between inlet and outlets—making it an attractive boundary condition candidate for simulations in complex vessel geometries.

We begin with a brief introduction to LBM. In Section 3 we introduce our scheme for the inlet. In Section 4, we demonstrate its capability to produce very accurate simulation results. A further discussion on the results is presented in Section 5. Finally, a summary is presented.

2. LATTICE-BOLTZMANN METHOD

In the standard LBM, the computational domain is discretized with a uniform lattice. We follow the convention, and apply LBM with dimensionless units, in which the uniform lattice spacing and discrete time step are set to unity, i.e. $\Delta x = 1$ and $\Delta t = 1$. Thus, the lattice velocity $c = \Delta x / \Delta t = 1$. Let

$$\mathscr{L} = [0, n_x - 1] \times [0, n_y - 1] \times [0, n_z - 1] \subset \mathbb{N}^3$$

denote the lattice with n_x, n_y, and n_z the number of lattice nodes in each spatial direction. Thus, the lattice nodes have integer coordinates: $\mathbf{r} = (x, y, z) \in \mathscr{L}$. Lattice nodes are assigned as solid or fluid nodes according to the geometry. The time evolution of the fluid in LBM comprises of repeated streaming and collision steps. In the former step, fictitious fluid particles are streamed to the neighbouring lattice nodes, while in the latter one, collisions among the particles are modelled. We adopt a convention where, at each time step, streaming operation precedes collision. In a time step t, the instant after streaming operation but before collision is denoted by $t^\star$.

The dynamic variables in LBM are distribution functions $f(\mathbf{r}, t, \mathbf{c}_i) =: f_i(\mathbf{r}, t), i = 0, \ldots, b-1$. The distribution values describe the probability of finding, at an instant t, a (fictitious) particle at site $\mathbf{r}$ with velocity $\mathbf{c}_i$. In other words, at every lattice node there is one distribution value associated with each velocity vector $\mathbf{c}_i$. The number of velocity vectors representing the discrete velocity space is model dependent. In standard models, the vectors $\mathbf{c}_i$ serve as exact links between the neighbouring lattice nodes. We introduce our inlet boundary scheme by using the D3Q19 model, which has $b = 19$ discrete velocities, or so-called links [22]. However, our inlet scheme is general and can be used with other models.

We apply the so-called incompressible version (ILBM) of the D3Q19 model [23]. In ILBM, density is decomposed into constant and fluctuating part: $\rho = \rho_0 + \delta\rho$. The essence of the model is to neglect all the terms proportional to $\delta\rho(\mathbf{u})$ and $\delta\rho(\mathbf{u})^2$, which are of the order of $\mathscr{O}(Ma^3)$ or higher; $\mathbf{u}$ is the macroscopic fluid velocity. Here Mach number Ma is the ratio between the fluid velocity and the speed of sound. In particular, the above-mentioned terms are neglected in the equilibrium distribution after expanding the expression for the fluctuating density. When the procedure described is applied to the standard equilibrium function, we obtain

$$f_i^{\mathrm{eq}}(\rho, \mathbf{u}) = w_i \left(\rho + \rho_0 \left[\frac{(\mathbf{c}_i \cdot \mathbf{u})}{c_s^2} + \frac{(\mathbf{c}_i \cdot \mathbf{u})^2}{2c_s^4} - \frac{u^2}{2c_s^2} \right] \right) \tag{1}$$

DOI: 10.1002/fld

where $c_s = 1/\sqrt{3}$ is the speed of sound. The value of the weight factor w_i depends on the length of the vector $\mathbf{c}_i$ such that the discrete velocities having lengths 0, 1, and $\sqrt{2}$ are associated with weight factor values $\frac{1}{3}$, $\frac{1}{18}$ and $\frac{1}{36}$, respectively. The hydrodynamic variables, as well as the non-hydrodynamic ones, are the moments of the distribution functions in the velocity space. The basic hydrodynamic variables, the mass density ρ and the momentum density $\rho\mathbf{u}$, are calculated from the zeroth and first moments:

$$\rho(\mathbf{r},t) = \sum_i f_i(\mathbf{r},t)$$

$$\rho(\mathbf{r},t)\mathbf{u}(\mathbf{r},t) = \sum_i \mathbf{c}_i f_i(\mathbf{r},t)$$

However, in ILBM the momentum density is redefined as

$$\rho_0\mathbf{u}(\mathbf{r},t) = \sum_i \mathbf{c}_i f_i(\mathbf{r},t)$$

In this work, a two-relaxation-time (TRT) scheme is utilized: the relaxation time τ_e is for tuning the viscosity and τ_o is chosen so as to minimize the viscosity-dependence of the slip velocity [24]. Let index $-i$ denote such a link that $\mathbf{c}_i = -\mathbf{c}_{-i}$. TRT can be conveniently formulated by using concepts of symmetric (even) $\widehat{f_i} = (f_i + f_{-i})/2$ and anti-symmetric (odd) $\widetilde{f_i} = (f_i - f_{-i})/2$ functions. Most important properties of these functions are $f_i = \widehat{f_i} + \widetilde{f_i}$, $\widehat{f_i} = \widehat{f}_{-i}$, and $\widetilde{f_i} = -\widetilde{f}_{-i}$. Symmetric and anti-symmetric notations are applied also for equilibrium f_i^{eq} and non-equilibrium $f_i^{\mathrm{neq}} = f_i - f_i^{\mathrm{eq}}$ functions. Even and odd moments of symmetric and anti-symmetric functions vanish, respectively. The lattice-Boltzmann equation for TRT is

$$f_i(\mathbf{r}+\mathbf{c}_i, t+1) = f_i(\mathbf{r},t) - \lambda_e \widehat{f}_i^{\mathrm{neq}}(\mathbf{r},t) - \lambda_o \widetilde{f}_i^{\mathrm{neq}}(\mathbf{r},t) \tag{2}$$

where $\lambda_e = 1/\tau_e$. Viscosity-dependence is minimized by choosing $\lambda_o = 8(2-\lambda_e)/(8-\lambda_e)$ [24].

3. MASS-FLUX-BASED INLET BOUNDARY CONDITION

In what follows, we assume that there is a single inlet and it locates completely on one face of the computational domain, say $y = 0$. Let Γ_{in} refer to a set including all the fluid lattice nodes at the inlet, N_f to the number of nodes in this set, and $\mathbf{n}$ is the unit inward normal of the inlet face. We continue by stating the fundamental assumption for our scheme: at the inlet, the correct flow field is unidirectional and perpendicular to the inlet boundary. More precisely, we assume an inlet flow in the y-direction: in the direction of the inward normal. This implies that for a reasonable distance from the inlet, the geometry remains constant in the flow direction.

Let I denote an index set enumerating the discrete velocities for the D3Q19 model. At the inlet, D3Q19 model has five links pointing out of the computational domain and five links pointing towards the domain. For convenience, we denote these outbound and inbound links with index sets I_{out} and I_{in}, respectively. After the streaming step all the distribution values, except those associated with the inbound links, are known at the inlet. The task of the inlet boundary condition is to deduce the distribution values for the inbound links. Let $I_{\mathrm{kn}} = I \setminus I_{\mathrm{in}}$ include the indices of the links for which the distribution values are known at the inlet after the streaming step. Furthermore, we denote with $M(t^\star)$ the total mass related to the inlet nodes after the streaming step. The total

DOI: 10.1002/fld

mass $M(t^\star)$ is not completely determined due to the unknown distribution values related to the inbound links at the inlet. The total mass related to the known distribution values at the inlet is

$$M_{\mathrm{kn}}(t^\star)=\sum_{\mathbf{r}\in\Gamma_{\mathrm{in}}}\Delta x^3\sum_{i\in I_{\mathrm{kn}}}f_i(\mathbf{r},t^\star)=\sum_{\mathbf{r}\in\Gamma_{\mathrm{in}}}\Delta x^3\rho_{\mathrm{kn}}(\mathbf{r},t^\star)=\sum_{\mathbf{r}\in\Gamma_{\mathrm{in}}}m_{\mathrm{kn}}(\mathbf{r},t^\star) \tag{3}$$

where $\rho_{\mathrm{kn}}(\mathbf{r},t^\star)$ is the local density related to the known distribution values after the streaming step.

Additionally, we assume

$$\mathbf{c}_i\cdot\mathbf{n}=-c, i\in I_{\mathrm{out}} \quad \text{and} \quad \mathbf{c}_i\cdot\mathbf{n}=c, i\in I_{\mathrm{in}}$$

All standard lattice-Boltzmann models, e.g. D2Q9, D3Q19, and D3Q27, fulfil this condition. The above assumption is made only to simplify the following notation. Now the local outgoing mass flux for the inlet nodes, after the streaming step, is

$$q_{\mathrm{out}}(\mathbf{r},t^\star)=-\sum_{i\in I_{\mathrm{out}}}(\mathbf{c}_i\cdot\mathbf{n})f_i(\mathbf{r},t^\star)=c\sum_{i\in I_{\mathrm{out}}}f_i(\mathbf{r},t^\star)=c\cdot\rho_{\mathrm{out}}(\mathbf{r},t^\star)=c\cdot\frac{m_{\mathrm{out}}(\mathbf{r},t^\star)}{\Delta x^3}, \quad \mathbf{r}\in\Gamma_{\mathrm{in}} \tag{4}$$

The units for mass flux are mass per unit area per unit time—that is, the units of momentum density. The minus sign in front of the first sum is because we prefer to define q_{out} as a positive value: the outbound links have negative y component due to our choice of inlet boundary ($y=0$). Furthermore, the outgoing mass flow rate over the inlet boundary is

$$Q_{\mathrm{out}}(t^\star)=\sum_{\mathbf{r}\in\Gamma_{\mathrm{in}}}\Delta x^2 q_{\mathrm{out}}(\mathbf{r},t^\star)=\frac{M_{\mathrm{out}}(t^\star)}{\Delta t} \tag{5}$$

Our inlet scheme operates with a single parameter $\bar{u}_y$ which is the average velocity at the inlet. We utilize this information to deduce the target mass flow rate $Q=A_{\mathrm{in}}\rho_0\bar{u}_y$ over the inlet, where $A_{\mathrm{in}}=N_f\cdot\Delta x^2$. Note, that we have utilized the definition of momentum density given by ILBM, and that here Q is not dependent on time. The mass flow rate Q is also the difference between the incoming (unknown) and outgoing mass flow rates (known): $Q=Q_{\mathrm{in}}-Q_{\mathrm{out}}$. This gives an equation for the unknown incoming mass flow rate:

$$Q_{\mathrm{in}}(t^\star)=\frac{M_{\mathrm{in}}(t^\star)}{\Delta t}:=Q+Q_{\mathrm{out}}(t^\star) \tag{6}$$

We apply our definition for the incoming mass flow rate, Equation (6), to determine the total mass related to the inlet nodes after the streaming step:

$$M(t^\star):=M_{\mathrm{kn}}(t^\star)+M_{\mathrm{in}}(t^\star) \tag{7}$$

Our next endeavour is to formulate an expression for the unknown local incoming mass flux $q_{\mathrm{in}}(\mathbf{r},t^\star)=c\cdot\rho_{\mathrm{in}}(\mathbf{r},t^\star)$. As already described above, we restrict to a simple case: at the inlet, the correct flow field is assumed unidirectional (y-direction) and perpendicular to the inlet boundary. Owing to the assumption of zero flow in the plane of the inlet, there are no pressure gradients and therefore no density gradients in the plane directions. This implies a common density ρ_c for all inlet nodes. The common density is defined as the average density for the inlet nodes: $\rho_c(t^\star):=M(t^\star)/(N_f\cdot\Delta x^3)$. This implies that locally the condition $\rho_c(t^\star)=\rho_{\mathrm{in}}(\mathbf{r},t^\star)+\rho_{\mathrm{kn}}(\mathbf{r},t^\star)$

DOI: 10.1002/fld

must be satisfied, which gives the expression

$$\rho_{\text{in}}(\mathbf{r}, t^\star) := \rho_c(t^\star) - \rho_{\text{kn}}(\mathbf{r}, t^\star) \tag{8}$$

enabling the computation of local incoming mass flux $q_{\text{in}}(\mathbf{r}, t^\star)$. From the local mass fluxes we deduce, in accordance with ILBM, the local flow velocities:

$$\rho_0 u_y(\mathbf{r}, t^\star) := q_{\text{in}}(\mathbf{r}, t^\star) - q_{\text{out}}(\mathbf{r}, t^\star), \quad \mathbf{r} \in \Gamma_{\text{in}} \tag{9}$$

Now we address the question how to assign a value for the unknown distribution functions at the inlet. There are a number of ways to determine the unknown distribution values from the above expressions for the basic hydrodynamic variables. Typically velocity boundary conditions require at least the local flow velocities, which are now available. We promote a simple procedure which is easy to implement. At the inlet, the equilibrium parts of the unknown distribution values can be evaluated with the hydrodynamic variables $\rho_c^\star \equiv \rho_c(t^\star)$ and $u_y^\star \equiv u_y(\mathbf{r}, t^\star)$. The non-equilibrium parts for the unknown distribution values are approximated from the values associated with the outbound links. That is, we compute

$$f_{-i}^{\text{neq}}(\mathbf{r}, t^\star) = f_{-i}(\mathbf{r}, t^\star) - f_{-i}^{\text{eq}}(\rho_c^\star, (0, u_y^\star, 0)), \quad \mathbf{r} \in \Gamma_{\text{in}} \tag{10}$$

and set $f_i^{\text{neq}}(\mathbf{r}, t^\star) := f_{-i}^{\text{neq}}(\mathbf{r}, t^\star)$ in accordance with the first-order Chapman–Enskog expansion [24]. This finally completes the expression for the unknown distribution functions:

$$f_i(\mathbf{r}, t^\star) := f_i^{\text{eq}}(\rho_c^\star, (0, u_y^\star, 0)) + f_{-i}^{\text{neq}}(\mathbf{r}, t^\star), \quad i \in I_{\text{in}}, \ \ \mathbf{r} \in \Gamma_{\text{in}} \tag{11}$$

Our inlet boundary condition does not depend on any particular choice of relaxation scheme or no-slip boundary condition for the solid–fluid interface; they can be chosen independently. Figure 2 is a summary of our inlet scheme.

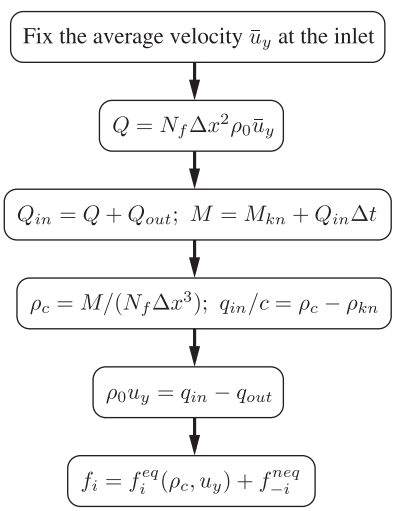

Figure 2. Summary of the proposed inlet boundary condition.

DOI: 10.1002/fld

4. NUMERICAL EXPERIMENTS

Here we demonstrate, numerically, the capabilities of the inlet scheme introduced in the previous section. First, we apply our scheme to flows in simple geometries, where analytical solutions are available. Then we proceed to more complex geometries representing some of the difficulties encountered in real simulations. For simplicity, we use geometries that are constant in the y-direction over the whole computational domain. That is, cross sections parallel to the inlet boundary are identical. At the solid–fluid interface, we apply the halfway bounce-back boundary condition [25, 26], i.e. the solid–fluid interfaces are located exactly halfway between adjacent lattice nodes. Furthermore, a scheme presented in Reference [21] is utilized at the outlet. In the analysis, we assess the non-local error of the simulated velocity using a relative L_2 norm defined as

$$L_2 = \frac{\sqrt{\sum (u_y - U_y)^2}}{\sqrt{\sum (U_y)^2}} \tag{12}$$

where $u_y(\mathbf{r}, t)$ denotes the simulated velocity and $U_y(\mathbf{r}, t)$ is the analytical solution.

4.1. Simple geometries with analytical solutions

To begin with, we compare the simulation results in simple geometries against the analytical solutions. Two configurations are selected: a channel flow, i.e. flow between two plates, and a pipe flow. In the former, the computational domain is confined in the z-direction by channel walls and periodic boundary conditions are applied in the x-direction. The inlet is at $y=0$ and a y-directional flow is considered. The analytical steady-state velocity profile for the channel flow is

$$U_y(z) = U_{\max}\left(1 - \left(\frac{z - c_z}{h}\right)^2\right)$$

where integer $c_z = (n_z + 1)/2$ is the z coordinate of the centerline, $h = n_z/2$ is half of the channel height, and $U_{\max} = \frac{3}{2}\bar{u}_y$ is the maximum velocity. For the pipe flow, the analytical steady-state velocity profile is

$$U_y(d) = U_{\max}\left(1 - \left(\frac{d}{R}\right)^2\right)$$

where $d(x, z) = \sqrt{(c_x - x)^2 + (c_z - z)^2}$ is the distance from the centerline, $R = D/2$ is the pipe radius, and $U_{\max} = 2\bar{u}_y$.

First, the effect of simulation parameters on the simulated velocity is considered. To this end, viscosity is varied by selecting five values for the relaxation time: $\tau_e \in \{0.6, 0.75, 1.0, 1.5, 2.0\}$. Furthermore, the value of average velocity $\bar{u}_y$ ranges from 0.00001 to 0.05. For all parameter values and for both channel and pipe flows, the L_2 norm at the inlet is plotted as a function of Reynolds number and shown in Figure 3. The definition for the Reynolds number is

$$Re = \frac{L\bar{u}_y}{\nu}$$

DOI: 10.1002/fld

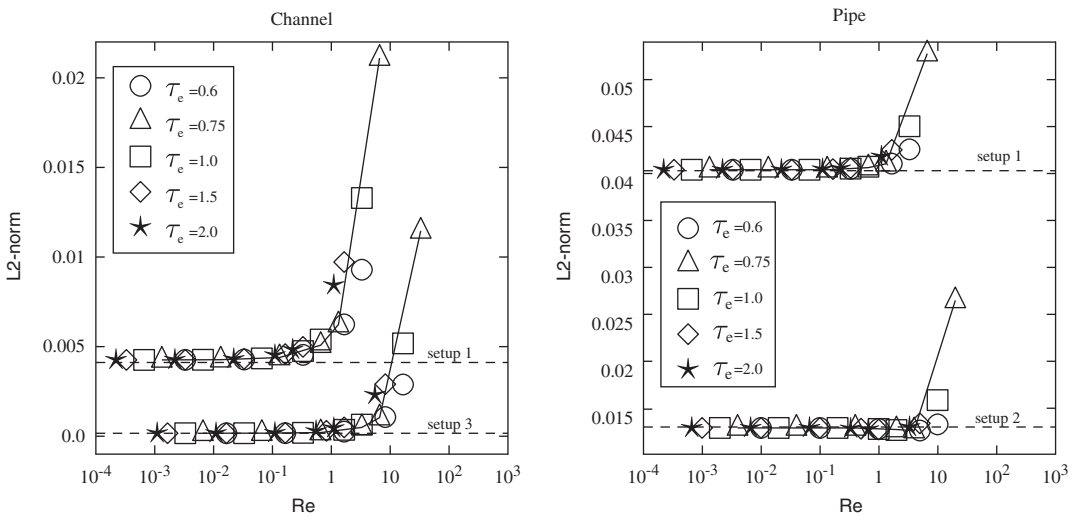

Figure 3. L_2 norms plotted as functions of Reynolds number at the channel inlets (left) and at the pipe inlets (right). Setups 1 and 3 are used for channel flows whereas setups 1 and 2 are used for pipe flows (see Table I). Value of the average velocity is between 0.00001 and 0.05.

Table I. Simulation setups for channel and pipe flows.

	Channel				Pipe				
Setup	n_x	n_y	n_z	Time steps	n_y	D	c_x	c_z	Time steps
1	3	51	11	10000	51	11	6	6	10000
2	3	153	33	30000	153	33	17	17	30000
3	3	255	55	50000	255	55	28	28	50000
4	3	459	99	100000	357	77	39	39	70000

where L is the channel height or pipe diameter, and v is the kinematic viscosity. In Figure 3, simulation setups 1 and 3 are used for the channel flow whereas setups 1 and 2 are used for the pipe flow (see Table I). Figure 3 reveals that error at the inlet, assessed by Equation (12), is almost independent of both relaxation time and average velocity when $Re \lesssim 1$. The exact value for the Reynolds number after which L_2 norm diverges depends on the discretization.

The spatial convergence of error for the inlet scheme in a channel and pipe flow is determined using the simulation setups defined in Table I; the converge rate at the inlet is approximately of second and first order for the channel and pipe flow, respectively (see Figure 4). These results agree with the convergence rates presented in the literature for LBM with the halfway bounce-back boundary condition (see Reference [27] and references therein). Thus, the inlet scheme does not degrade the spatial convergence rate of LBM. Moreover, the convergence rate does not depend on relaxation time nor average velocity as long as the Reynolds number in these measurements remains below one.

DOI: 10.1002/fld

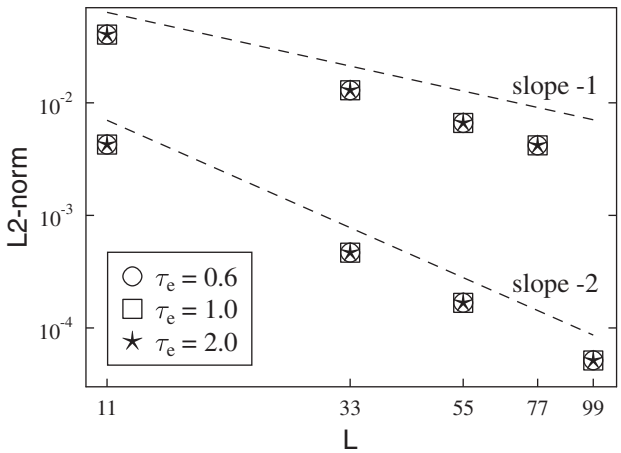

Figure 4. The spatial convergence of error in channel and pipe geometries. Average inlet velocity is fixed: $\bar{u}_y = 0.00001$. Symbols following the reference line with slope -2 and slope -1 are from channel and pipe geometries, respectively. On the horizontal axis, L refers to channel height and pipe diameter.

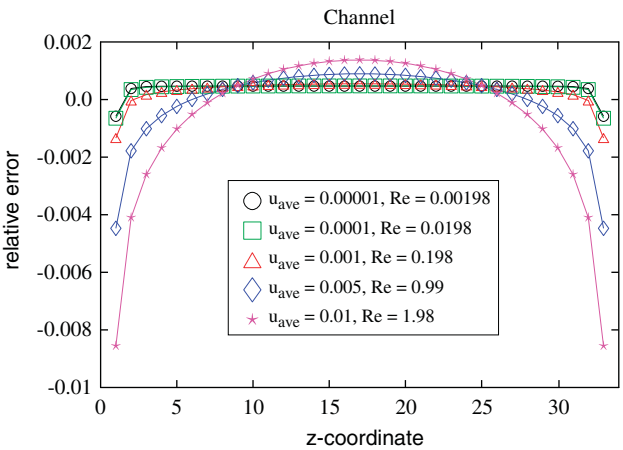

Figure 5. Relative error of the simulated velocity at the inlet of the channel. Setup 2 is used with relaxation time $\tau_e = 1.0$.

Figure 5 presents the relative error of the simulated velocity at the inlet of the channel. Here setup 2 is used with relaxation time $\tau_e = 1.0$. The relative error is calculated locally as

$$u_{\text{err}}(z) = \frac{U_y(z) - u_y(z)}{U_y(z)} \tag{13}$$

The relative error increases when average velocity, and thus Reynolds number, is increased. The relative error is largest close to the channel walls. However, the relative error remains below one percent even for $\bar{u}_y = 0.01$ ($Re = 1.98$).

DOI: 10.1002/fld

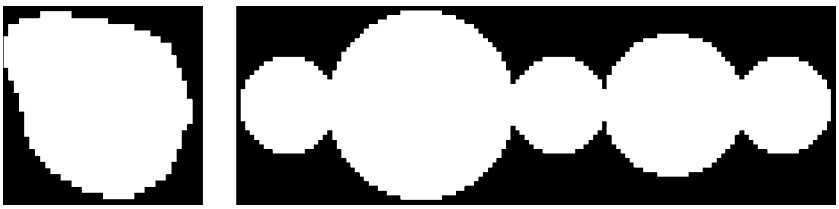

Figure 6. Two inlet geometries: a cross section of an abnormal vessel (left) and a row of intersecting circles (right).

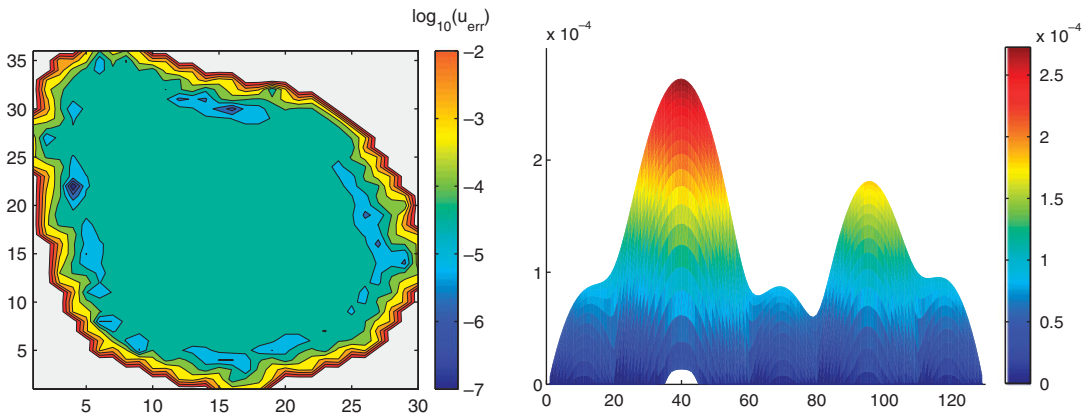

Figure 7. On the left, the local relative error calculated at the inlet with Equation (14) is presented for the vessel geometry in logarithmic scale. The projected velocity profile at the inlet for row of intersecting circles is presented at the right.

4.2. Complex inlet geometries

In the following our aim is to demonstrate that the present inlet scheme is capable of producing velocity profiles which convincingly adapt to the complex inlet geometries—without *a priori* information about the local inlet velocity values nor about the pressure gradients for the system.

For this purpose we have selected two inlet geometries: a cross section of an abnormal vessel in a tumour vascular system and a row of intersecting circles (cf. Figure 6). The staircase pattern of geometries, evident in Figure 6, is inherent when the halfway bounce-back boundary condition is utilized. More elaborate boundary conditions would dramatically smooth out the solid–fluid interfaces perpendicular to the inlet [28–30]. However, here we concentrate on the inlet boundary condition and settle for the halfway bounce-back boundary condition at the solid–fluid interfaces. In these complex geometries, flows are simulated with $\tau_e = 1.0$ and $\bar{u}_y = 0.0001$. Simulations are run until a steady state is reached. We assess the simulated inlet velocity profile by comparing it with the velocity profile obtained from the halfway in flow direction (i.e. from the cross section at $y = n_y/2$). That is, we compute the local relative error by using the velocities from the halfway

DOI: 10.1002/fld

as a reference:

$$u_{\mathrm{err}}(x,z)=\left|\frac{u_y^r(x,z)-u_y(x,z)}{u_y^r(x,z)}\right| \tag{14}$$

where the vertical bars denote the absolute value and u^r is the reference velocity from the halfway.

In Figure 7, the relative error at the inlet is presented for the vessel geometry in a logarithmic scale. Length of the domain in the flow direction, $n_y=151$, is chosen so that the error norm (14) is meaningful. The error is largest close to the solid boundaries where it has a magnitude of the order of one percent. In the bulk of the fluid domain, the relative error is two to three orders of magnitude smaller. The projected velocity profile at the inlet for the row of intersecting circles is presented in Figure 7. It is yet an another demonstration that the inlet scheme is capable of producing a velocity field that conforms to the geometry and is accurate even at the inlet.

5. DISCUSSION

Comparison of simulated velocity profiles against analytical solutions reveal a very good agreement. However, divergence of the relative L_2 error norm value occurs when $Re\gtrsim 1$. Origin of the divergence is currently unknown, but one might suspect that it is related to the approximation chosen for the non-equilibrium parts of the unknown distribution functions which does not take into account the high-order corrections. If the divergence turns out to emerge from the non-equilibrium approximation, a more elaborate approximation will improve the accuracy of flow simulations with higher Reynolds number.

Be that as it may, in practice our scheme is not limited to simulations where $Re\lesssim 1$. First of all, the mass flow rate remains correct at the inlet despite of errors in local velocities. Second, errors in local velocities are small for practical purposes even with moderate Reynolds number ($1\lesssim Re\lesssim 100$). This is evident from Figure 5 and especially from Table II where relative error of maximum velocity is given for three channel flow simulations. Setup 3 is used, $\tau_e=0.6$, and average inlet velocity is varied. Relative error of maximum velocity is computed with Equation (13) at the inlet and in the middle of the flow domain. When $Re=82.5$, the error at the inlet is approximately 4%—a small number in many applications. As a final argument, by presenting errors computed directly at the inlet, we give the most critical view on the proposed inlet scheme. Errors computed

Table II. Relative error of the maximum velocity in channel flow simulations.

	Relative error of $u_{\max}$	
Re	Inlet	Middle
0.0165	0.000168	0.000164
1.65	0.000314	0.000163
82.5	0.0408	0.00479

Setup 3 is used with $\tau_e=0.6$: value of the average inlet velocity varies. Errors are computed at the inlet and in the middle of the flow domain.

DOI: 10.1002/fld

inside the flow domain are smaller. This is also apparent from Table II. Relative error of the maximum velocity in the middle of the flow domain is less than 5 per mil for the largest Reynolds number.

We give the last remark prior to the summary: the inlet density and local inlet velocities evolve in time before converging to the steady-state values. During time evolution, we observe clear oscillations specifically in density (pressure) field. Oscillations are largest at the beginning of the simulations and are presumably amplified by poor initial conditions.

6. SUMMARY

We have presented a mass-flux-based inlet scheme for lattice-Boltzmann flow simulations. It requires minimal amount of boundary data, namely the average velocity at the inlet. By comparing the simulated velocities against analytical solutions in simple geometries, we have shown that our scheme produces results that are accurate at the inlet. Furthermore, the analysis of the results in simple geometries reveals that the error is related to the Reynolds number. The error in simulated velocity is almost independent of relaxation time and average velocity if $Re \lesssim 1$. The exact value of Reynolds number after which the error diverges is dependent on discretization. However, even with moderate Reynolds number, the error remains reasonable for many practical applications.

In addition, simulations in geometries obtained from a cross section of a vessel and from a row of intersecting circles further demonstrate the capability of our scheme to produce velocity profiles at the inlet which faithfully conform to the complex geometries. In addition, from a practical point of view, our inlet scheme has the desirable property that, since the average velocity is assigned, the Reynolds number value for the simulation is obtained by simply measuring the characteristic length scale at the inlet. Our future endeavours include modification of the inlet scheme presented here, to flows which are not unidirectional at the inlet, i.e. for flows in inclined channels and pipes.

ACKNOWLEDGEMENTS

We are grateful to Viivi Koivu MSc for her valuable contribution in the preparation of this article. Furthermore, we express our sincere gratitude to Professor Jussi Timonen for his constant support. This work was supported by the Academy of Finland (Project No. 7117283).

REFERENCES

1. Chen S, Doolen GD. Lattice Boltzmann method for fluid flows. *Annual Review of Fluid Mechanics* 1998; **30**:329–364.
2. Succi S. *The Lattice Boltzmann Equation for Fluid Dynamics and Beyond*. Oxford University Press: Oxford, 2001.
3. Koponen A, Kandhai D, Hellén E, Alava M, Hoekstra A, Kataja M, Niskanen K, Sloot P, Timonen J. Permeability of three-dimensional random fiber webs. *Physical Review Letters* 1998; **80**(4):716–719.
4. Ladd AJC. Numerical simulations of particulate suspensions via a discretized Boltzmann equation. Part 1. Theoretical foundation. *Journal of Fluid Mechanics* 1994; **271**:285–309.
5. Hirabayashi M, Ohta M, Rufenacht DA, Chopard B. A lattice Boltzmann study of blood flow in stented aneurism. *Future Generation Computer Systems* 2004; **20**(6):925–934.
6. Deschamps T, Schwartz P, Trebotich D, Colella P, Saloner D, Malladi R. Vessel segmentation and blood flow simulation using level-sets and embedded boundary methods. *International Congress Series* 2004; **1268**:75–80.
7. Artoli AM, Hoekstra AG, Sloot PMA. Mesoscopic simulations of systolic flow in the human abdominal aorta. *Journal of Biomechanics* 2006; **39**(5):873–884.

DOI: 10.1002/fld

8. Mabotuwana TDS, Cheng LK, Pullan AJ. A model of blood flow in the mesenteric arterial system. *Biomedical Engineering Online* 2007; **6**:17.
9. Bernsdorf J, Harrison SE, Smith SM, Lawford PV, Hose DR. Applying the lattice Boltzmann technique to biofluids: a novel approach to simulate blood coagulation. *Computers and Mathematics with Applications* 2008; **55**(7):1408–1414.
10. Sun C, Munn LL. Lattice-Boltzmann simulation of blood flow in digitized vessel networks. *Computers and Mathematics with Applications* 2008; **55**(7):1594–1600.
11. Leunig M, Yuan F, Menger MD, Boucher Y, Goetz AE, Messmer K, Jain RK. Angiogenesis, microvascular architecture, microhemodynamics, interstitial fluid pressure during early growth of human adenocarcinoma LS174T in SCID mice. *Cancer Research* 1992; **52**(23):6553–6560.
12. Yuan F, Salehi HA, Boucher Y, Vasthare US, Tuma RF, Jain RK. Vascular permeability and microcirculation of gliomas and mammary carcinomas transplanted in rat and mouse cranial windows. *Cancer Research* 1994; **54**(17):4564–4568.
13. Kobayashi H, Takizawa N, Negishi T, Tanishita K. Intravascular inhomogeneous oxygen distribution in microvessels: theory. *Respiratory Physiology and Neurobiology* 2002; **133**(3):271–275.
14. Bloor MIG. The flow of blood in the capillaries. *Physics in Medicine and Biology* 1968; **13**(3):443–450.
15. Maier RS, Bernard RS, Grunau DW. Boundary conditions for the lattice Boltzmann method. *Physics of Fluids* 1996; **8**(7):1788–1801.
16. Zou Q, He X. On pressure and velocity boundary conditions for the lattice Boltzmann BGK model. *Physics of Fluids* 1997; **9**(6):1591–1598.
17. Inamuro T, Yoshino M, Ogino F. A non-slip boundary condition for lattice Boltzmann simulations. *Physics of Fluids* 1995; **7**(12):2928–2930.
18. Yu D, Mei R, Shyy W. Improved treatment of the open boundary in the method of lattice Boltzmann equation: general description of the method. *Progress in Computational Fluid Dynamics* 2005; **5**(1/2):3–12.
19. Freitas R, Schröder W. Numerical investigation of the three-dimensional flow in a human lung model. *Journal of Biomechanics* 2008; **41**(11):2446–2457.
20. Chen S, Martínez D, Mei R. On boundary conditions in lattice Boltzmann methods. *Physics of Fluids* 1996; **8**(9):2527–2536.
21. Chikatamarla SS, Ansumali S, Karlin IV. Grad's approximation for missing data in lattice Boltzmann simulations. *Europhysics Letters* 2006; **74**(2):215–221.
22. Qian YH, d'Humières D, Lallemand P. Lattice BGK models for Navier–Stokes equation. *Europhysics Letters* 1992; **17**:479–484.
23. He X, Luo L-S. Lattice Boltzmann model for the incompressible Navier–Stokes equation. *Journal of Statistical Physics* 1997; **88**(3–4):927–944.
24. Ginzburg I, d'Humières D. Multireflection boundary conditions for lattice Boltzmann models. *Physical Review E* 2003; **68**(6):066614.1–066614.30.
25. Wolfram S. Cellular automaton fluids. I. Basic theory. *Journal of Statistical Physics* 1986; **45**(3–4):471–526.
26. Lavallée P, Boon JP, Noullez A. Boundaries in lattice gas flows. *Physica D*: *Nonlinear Phenomena* 1991; **47**(1–2):233–240.
27. Yu D, Mei R, Luo L-S, Shyy W. Viscous flow computations with the method of lattice Boltzmann equation. *Progress in Aerospace Sciences* 2003; **39**:329–367.
28. Noble DR, Torczynski JR. A lattice-Boltzmann method for partially saturated computational cells. *International Journal of Modern Physics C* 1998; **9**(8):1189–1201.
29. Strack OE, Cook BK. Three-dimensional immersed boundary conditions for moving solids in the lattice-Boltzmann method. *International Journal for Numerical Methods in Fluids* 2007; **55**(2):103–125.
30. Bouzidi M, Firdaouss M, Lallemand P. Momentum transfer of a Boltzmann-lattice fluid with boundaries. *Physics of Fluids* 2001; **13**(11):3452–3459.

DOI: 10.1002/fld